Vietnam Journal of Science and Technology
DOI: https://doi.org/10.15625/2525-2518/20279

Structural characterization and electrochemical properties of MoS_2/graphene oxide nanocomposite for supercapacitor application

Le Ngoc Long[1,2,3], Tran Van Khai[1,2,4,*]

[1]*Faculty of Materials Technology, Ho Chi Minh City University of Technology (HCMUT), 268 Ly Thuong Kiet Street, Dien Hong Ward, Ho Chi Minh City, Viet Nam*
[2]*Vietnam National University - Ho Chi Minh City (VNU-HCM), Quarter 33, Linh Xuan Ward, Ho Chi Minh City, Viet Nam*
[3]*School of Applied Chemistry, Tra Vinh University, 126 Nguyen Thien Thanh street, Hoa Thuan Ward, Vinh Long Province, Viet Nam*
[4]*VNU-HCM Key Laboratory for Material Technologies, Ho Chi Minh City University of Technology (HCMUT), 268 Ly Thuong Kiet Street, Dien Hong Ward, Ho Chi Minh City, Viet Nam*

*Email: *tvkhai1509@hcmut.edu.vn*

Received: 6 March 2024; Accepted for publication: 25 July 2024

Abstract. Supercapacitors and micro-supercapacitors are promising capacitive energy storage devices for portable electronics and microelectromechanical systems. However, their low volumetric energy and power density as compared to batteries might limit them from many practical applications. In this research, the low-dimension MoS_2/graphene oxide nanocomposite (MoS_2/C NC) was successfully synthesized by a simple hydrothermal approach and utilized as an electrode material for supercapacitor applications. The obtained materials were systematically investigated by various characterization techniques. FE-SEM and HR-TEM were employed to examine the surface morphology, microstructure, and crystallite size. Meanwhile, XRD, EDS, XPS, Raman spectroscopy, and FTIR spectroscopy were used to determine the phase and chemical composition of the synthesized samples. The electrochemical capacitance properties were measured by CV and EIS techniques. FE-SEM and HR-TEM results reveal that ultrathin two-dimensional MoS_2 crystals were grown *in-situ* on the graphene oxide surface, forming a porous three-dimensional (3D) architecture. The thickness and average lateral size of MoS_2 crystals determined by HR-TEM were around ~1.8–3.5 nm (~3–6 nm layers) and ~200–300 nm, respectively. The results of XRD, Raman, and XPS studies confirm that the as-grown MoS_2 crystals have a predominantly hexagonal phase structure (2H-MoS_2). The thin-film electrode based on MoS_2/ NC exhibits a high specific capacitance of ~118.5 F g^{-1} at 1 A g^{-1}, along with a large electrochemically active surface area of ~218.0 m^2 g^{-1}. It also delivers a high energy density of ~88.0 Wh kg^{-1} and a power density of ~367.0 W kg^{-1}. Combined with its low charge-transfer resistance, these features highlight the strong potential of the synthesized MoS_2/C NC for supercapacitor applications.

Keywords: MoS_2, graphene, nanocomposite, electrochemical, supercapacitor.

Classification numbers: 2.4.4, 2.8.3, 2.9.4.

1. INTRODUCTION

Controlling the electrostatic charge and discharge of the electrochemical double layer at the electrode–electrolyte interface of high–specific surface area materials is crucial for energy storage devices such as supercapacitors. These devices store energy through the formation of a charged double layer of electrolyte ions on the surface of the electrode materials [1]. Therefore, the charge density or energy density of a supercapacitor depends mainly on the surface area of the electrode materials. The performance of supercapacitors is influenced by several factors, including electrode materials, separators, electrolytes, and fabrication techniques [2]. Among these, electrode materials play a dominant role in determining capacitance and energy density. Therefore, an effective strategy to enhance energy density is to employ electrode materials with a high specific surface area.

In this regard, graphene - a monolayer of carbon atoms covalently bonded through sp^2 hybridization in a hexagonal crystalline lattice - has attracted significant attention due to its outstanding physicochemical properties [3]. These include a high charge carrier mobility of ~2×10^5 cm^2 V^{-1} s^{-1} [4, 5], a large specific surface area of ~2630 m^2 g^{-1} [6], and semi-metallic behavior with a zero bandgap [5], which are advantageous for controlling the electrostatic charge and discharge of the electric double layer at the electrode–electrolyte interface. Such interesting physical properties that turn graphene to become a promising platform for various applications, including fuel cells [7], Li-ion batteries [8, 9], and supercapacitors [7, 10]. Unfortunately, graphene exhibits low efficiency in supercapacitors due to its insufficient charge-storage capability.

Recently, molybdenum disulfide (MoS_2) has emerged as one of the most attractive two-dimensional (2D) materials, belonging to the transition metal dichalcogenide family [11]. Like graphene, 2D-MoS_2 exhibits a layered (lamellar) structure in which molybdenum (Mo) atoms are covalently bonded to sulfur (S) atoms, forming a monolayer with an S–Mo–S configuration. These monolayers stack together via weak van der Waals interactions along the [001] direction, forming bulk MoS_2 crystals [12]. MoS_2 exhibits its charge storage capability by forming electric double-layers of charged carriers at their contact interface with electrolytic medium (double-layer capacitance mechanism) and by faradaic charge transfer interlayer or intralayer on the Mo centers whose oxidation states can occupy between +2 and +6 (pseudo-capacitance mechanism). These characteristics result in significantly high energy density for supercapacitor applications with unlimited charging/discharging cycles. Nevertheless, low carrier mobility of 2D-MoS_2 (~0.5–3.0 cm^2 V^{-1} s^{-1}) material limits most of its efficiency in such energy storage devices as batteries or supercapacitors [13]. Very recently, the incorporation of MoS_2 into graphene or graphene oxide (GO) has attracted significant attention due to the enhanced performance and stability of the resulting composites across a wide range of applications, including energy storage/conversion and biomedical fields [14,15]. It is expected that the combination of two of these materials from van der Waals solids or from the covalent bonding materials will allow full use of their advantages and mitigate their disadvantages [16]. Currently, various methods have been developed to synthesize MoS_2/graphene composites, such as solvothermal, hydrothermal [17-20], chemical vapor deposition [21], van der Waals epitaxy [22], sonication [23], microwave [24], and liquid-phase exfoliation [25]. Among them, hydrothermal method is the most common method to prepare MoS_2/graphene composites. This method offers several advantages, including relatively low synthesis temperatures and pressures, uniform mixing of precursors, and precise control over the morphology and size of both MoS_2 and GO components. It is also suitable for large-scale production and enables the uniform dispersion of MoS_2 on graphene sheets, thereby enhancing

interfacial interactions and overall material properties. Therefore, it is expected to become one of the primary approaches for industrial production of high-performance MoS_2/GO nanocomposites. In this research, we propose a simple hydrothermal method in which nanostructured 2D-MoS_2 crystals were grown on GO nanosheets to produce MoS_2/C NC material. We then studied the specific capacitance and electrochemical characteristics of a thin film electrode made from the resulting MoS_2/C NC for supercapacitor applications. Interestingly, incorporating nanocrystalline 2D-MoS_2 structures into the GO matrix leads to a significant enhancement in the specific capacitance of the resulting MoS_2/C nanocomposite electrode, along with excellent cycling stability and low electrical resistance. This opens the prospect of its employment in supercapacitor applications.

2. MATERIALS AND METHODS

2.1. Materials

Graphite powder (99.8 %) was commercially obtained from Sigma-Aldrich (St. Louis, MO, USA). Concentrated phosphoric acid (H_3PO_4, 85 %), sulfuric acid (H_2SO_4, 98 %), potassium permanganate ($KMnO_4$, 98 %), hydrogen peroxide (H_2O_2, 30 wt%), ammonium molybdate tetrahydrate ($(NH_4)_6Mo_7O_{24}.4H_2O$, 98 %), thioacetamide (CH_3CSNH_2, 98 %), and ammonia solution (NH_4OH, 25 wt%) were purchased from Merck Chemicals Co., Ltd. (Germany). Deionized water (Milli-Q, 18 MΩ·cm) was provided by Millipore Corp., Billerica (MA, USA). All reagents used in the experiments were of analytical grade and were used without further purification.

2.2. Fabrication of MoS_2/graphene oxide nanocomposites (MoS_2/C NCs)

In this work, in the first step, the GO nanosheets were synthesized from the chemical oxidation of graphite flakes with $KMnO_4$ in a mixture solution containing H_2SO_4 and H_3PO_4. Details of the GO synthesis process are presented in [26-29]. Then, the MoS_2/graphene oxide nanocomposites (MoS_2/C NCs) with molar ratio of Mo^{4+} (~1.5):C (~1) were synthesized by a simple hydrothermal technique. Briefly, an amount of ~0.1506 gram of $(NH_4)_6Mo_7O_{24}.4H_2O$ and 0.3069 gram of CH_3CSNH_2 were added to a volume ~100 mL of GO (~1.0 g L^{-1}) dispersion, and then submitted to ultrasonication in bath water for ~1 hour (at 37 kHz, kept at ~30 °C), resulting in a homogeneous suspension. The obtained suspension was then adjusted to pH of ~5–6 by addition of an appropriate volume of NH_3 solution. Next, the mixture was transferred into a 125 mL Teflon-lined stainless steel autoclave reactor (Parr Instrument Company, Moline, IL, USA, ~80 % volume filled) and heated at 230 °C for 2 hours with a heating rate of ~10 °C min^{-1}. After that, the autoclave reactor was removed from the furnace and allowed to cool naturally to ambient temperature. Then, the synthesized products were washed multiple times with deionized water and ethanol solution before being collected by centrifugation. Finally, the resultant products were dried in a vacuum furnace at 60 °C for 24 hours before being utilized to characterize the properties. For comparison, bare MoS_2 nanocrystals were prepared under identical conditions, except that the GO dispersion was omitted from the precursor solution.

2.3. Characterization

2.3.1. Morphology and microstructure

The crystal structure and phase composition of the MoS_2/C NCs were analyzed by X-ray diffraction (XRD) using a Bruker D8 Advance diffractometer (Bruker, Germany) with CuKα radiation (λ = 1.54178 Å), operated at 40 kV and 200 mA. Data were collected over a 2θ range of 5–70°, with a step size of 0.0194° in continuous scanning mode. The morphology and structural features of MoS_2/C NCs were examined using a JEOL JEM-2010 high-resolution transmission electron microscope (HR-TEM, JEOL Ltd., Tokyo, Japan) operated at an accelerating voltage of 200 kV. The chemical composition and elemental mapping were characterized using scanning transmission electron microscopy (STEM, JEM-ARM200F, JEOL Ltd., Japan) operated at 200 kV and equipped with energy-dispersive X-ray spectroscopy (EDS, JED-2300, JEOL, Japan). The morphology of GO and the MoS_2/C samples was investigated using field-emission scanning electron microscopy (FE-SEM, Hitachi S-4800, Japan) operated at an accelerating voltage of 10 kV. Fourier transform infrared (FTIR) spectroscopy (PerkinElmer Spectrum, USA) was employed to confirm the presence of functional groups on the sample surfaces. The spectra were recorded in the range of 400-4000 cm^{-1}. Raman spectra were recorded over the frequency range of 100–3000 cm^{-1} using a Micro Raman Horiba XploRA One instrument equipped with a green argon laser (λ = 532 nm) as the excitation source. The surface composition and chemical states of the GO and MoS_2/C samples were studied by X-ray photoelectron spectroscopy (XPS, VG Multilab ESCA 2000 system, UK) using Al Kα radiation (hν = 1486.6 eV) as the excitation source. The XPS spectra were analyzed using XPSPEAK41 software, employing a Gaussian–Lorentzian sum function after Shirley background subtraction.

2.3.2. Electrode fabrication and electrochemical measurements

Cyclic voltammetry (CV) and electrochemical impedance spectroscopy (EIS) measurements were performed at room temperature using a PGSTAT302N electrochemical workstation (Metrohm, Switzerland), operated with NOVA v2.1.3 software. A three-electrode electrochemical system was employed, consisting of a working electrode (WE) prepared by coating MoS_2/C nanocomposite (~91.0 wt.%) and carbon black (~6.0 wt.%) onto a 6 mm diameter glassy carbon electrode (CH Instruments, TX, USA), an Ag/AgCl (3 M KCl) reference electrode (RE), and a Pt counter electrode (CE). All chemicals used in the electrochemical measurements were purchased from Sigma-Aldrich (St. Louis, MO, USA). For CV measurements, a 1 M Na_2SO_4 solution was used as an electrolyte. The CV tests were conducted over a potential window of −1.2 to 0.2 V at various scan rates ranging from 5 to 100 mV s^{-1}. The specific capacitance (C_{sp}) of the fabricated MoS_2/C NC electrodes can be evaluated by Eq. (1) or Eq. (2):

$$C_{sp} = \frac{|Q_A| + |Q_C|}{2m \times \Delta V}, \text{ F g}^{-1} \quad (1)$$

where Q_A and Q_C are the charges storage at the anode and cathode, respectively; m (g) is the mass of the electrode materials; and ΔV (V) is the potential window of the CV curve. The energy density E (Wh kg^{-1}) and power density P (W kg^{-1}) were calculated from the CV curves according to Eqs. (3) and (4) in which v (mV s^{-1}) is the scan rate,

$$C_{sp} = \frac{Q}{2V} = \frac{1}{2V\nu}\int_{V^-}^{V^+} i(V)dV, \text{ F g}^{-1} \quad (2)$$

$$E = \frac{1}{2} C_{sp} (\Delta V)^2, \text{ Wh kg}^{-1} \tag{3}$$

$$P = \frac{1}{2} C_{sp} (\Delta V) \nu, \text{ W kg}^{-1} \tag{4}$$

The EIS measurements were carried out over a frequency range of 99 kHz to 0.01 Hz at open-circuit potential, using an AC voltage amplitude of 10 mV. The impedance measurements were conducted in a 0.1 M KCl solution containing 5 mM ferro/ferricyanide. Deionized water was used for all cleaning and solution preparations. The electrode capacitance $C(\omega)$ is composed of real part $C'(\omega)$ (Eq. (5)) and the imaginary part $C''(\omega)$ (Eq. (6)) components.

$$C'(\omega) = \frac{-Z''(\omega)}{\omega |Z(\omega)|^2} \tag{5}$$

$$C''(\omega) = \frac{Z'(\omega)}{\omega |Z(\omega)|^2} \tag{6}$$

Electrochemical surface of the electrode material can be calculated by the formula (7) in which C_d is constant value of 20 μF cm^{-2} [30] and C_{dm} is calculated by Eq. (8), where Z'' is the imaginary part of impedance value calculated at responded frequency $f \sim 0.01$ Hz, and m (g) is the mass of the electrode materials.

$$S_E = \frac{C_{dm}}{C_d}, \text{ m}^2 \text{ g}^{-1} \tag{7}$$

$$C_{dm} = \frac{1}{2m\pi f Z''}, \text{ F g}^{-1} \tag{8}$$

$$\tau_o = \frac{1}{2\pi f_o}, \text{ s} \tag{9}$$

The relaxation time constant τ_o (s) is defined as the minimum time needed to discharge the entire energy stored in the device with an efficiency over 50 % [31] and calculated by Eq. (9) with f_o is the knee frequency at which the imaginary component of the impedance reaches the highest value in the high frequency (HF) region [32].

3. RESULTS AND DISCUSSION

3.1. Structures, morphologies, and chemical compositions of GO and MoS_2/C NC

The surface morphology and structural characteristics of the as-prepared GO sheets have been evaluated by FE-SEM and TEM. As shown in Figure 1(a), the FE-SEM image indicates that the GO material exhibits a layered morphology, consisting of individual GO sheets loosely interconnected to form a three-dimensional network structure. Figure 1(b) shows that single- and/or few-layer GO sheets with characteristic wrinkled features are obtained after the ultrasonication process. The edges of the GO nanosheets are slightly curved due to surface tension and the presence of oxygen-containing functional groups on their surfaces and edges. A paper-like morphology of ultrathin GO nanosheets is observed in the TEM image (Figure 1(c)), where

transparent sheets with typical wrinkled and crumpled features can be seen. The TEM results indicate that the GO nanosheets have lateral dimensions ranging from a few to several micrometers. These observations confirm the successful synthesis of GO nanosheets via chemical oxidation of graphite flakes.

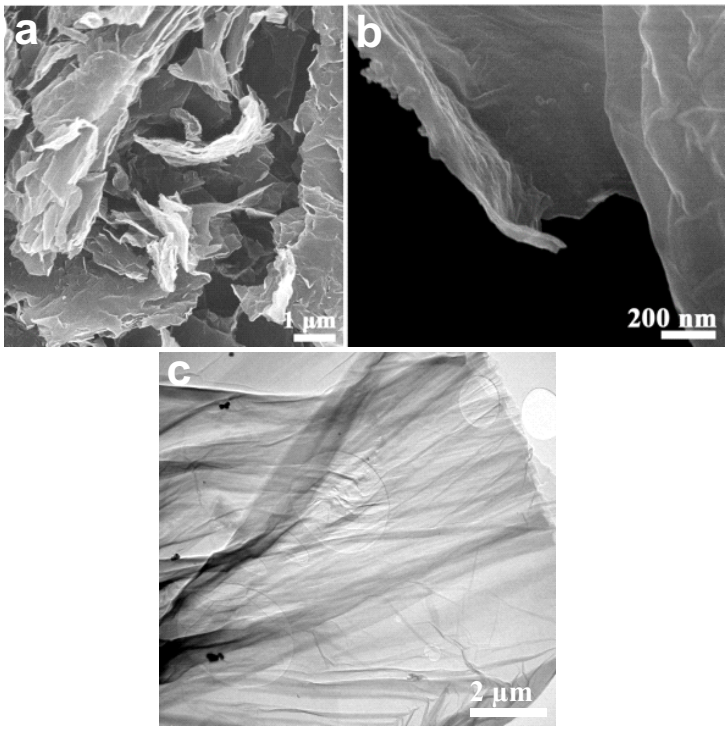

Figure 1. FE-SEM images of the as-prepared GO nanosheets at (a) low and (b) high magnifications, along with (c) a TEM image.

The crystalline structures of the prepared MoS_2/C NC, GO, and bare MoS_2 samples were investigated by XRD, as shown in Figure 2(a). The XRD pattern of GO exhibits two distinct peaks at 2θ ≈ 10.6° and 23.4°, corresponding to the (001) and (002) crystal planes, respectively. These diffraction peaks are in good agreement with the standard JCPDS data (JCPDS No. 00-065-1528), confirming the successful synthesis of GO. For the MoS_2/C NC sample, the XRD pattern exhibits diffraction peaks at 2θ ≈ 14.3°, 33.1°, 40.1°, 49.3°, and 59.1°, which are indexed to the (002), (100), (103), (105), and (110) crystal planes of MoS_2, respectively. These reflections are consistent with the standard diffraction pattern of hexagonal 2H-MoS_2 (JCPDS No. 00-037-1492) and are in good agreement with those observed for the bare MoS_2 sample reported in previous studies [17–20], confirming the successful formation of MoS_2/C NC. Notably, no additional diffraction peaks are observed, indicating the high phase purity of the as-prepared samples. It can be noticed that the strong diffraction peak centered at $2\theta \approx 14.3°$ of the (002) plane corresponds to the lattice plane distance $d_{(002)}$ ~0.63 nm (calculated using Bragg's equation [33]), which represents interlayer spacing of a stacked MoS_2 structure [19, 34, 35], indicating that 2D-MoS_2 crystals grew on the surfaces of GO sheets along the preferred direction of [001], as found in the literature [36, 37]. Compared to the initial GO pattern, the characteristic diffraction peaks at 2θ ≈ 10.6° and 23.4° almost disappear in the XRD pattern of MoS_2/C NC. This indicates that GO was effectively reduced to reduced graphene oxide (rGO) during the synthesis process [38]. However, the characteristic diffraction peak of rGO, typically observed in the range of 2θ ≈ 25.4–

26.2°, is not clearly detected. This absence may be attributed to the low content of rGO and/or its relatively low degree of crystallinity compared with MoS_2 crystals. In addition, the growth and anchoring of MoS_2 crystals on the rGO surface likely disrupt the regular stacking of rGO layers, leading to a more disordered structure within the composite. Similar observations have been reported in previous studies [19, 39]. Based on the XRD analysis, it can be concluded that the optimal reaction temperature and reaction time for the growth of 2D MoS_2 nanostructures on rGO are 230 °C and 2 hours, respectively [40].

The formation mechanism of 2D-MoS_2 nanostructures in-situ on GO in the hydrothermal process can be described as the reduction of MoO_4^{2-} ions by HS^- ions to form MoS_3 according to Eq. (10) to Eq. (13), followed by the phase transformation of MoS_3 to MoS_2 as described by Eq. (14).

$$(NH_4)_6Mo_7O_{24}.4H_2O \rightarrow MoO_4^{2-} + NH_3 + H_2O \quad (10)$$

$$CH_3CSNH_2\ (s) + 2H_2O \rightarrow CH_3COO^- + 2H^+ + NH_4^+ + HS^- \quad (11)$$

$$MoO_4^{2-} + 4HS^- \rightarrow MoS_4^{2-} + 4OH^- \quad (12)$$

$$MoS_4^{2-} + H^+ \rightarrow MoS_3 + HS^- \quad (13)$$

$$MoS_3 \rightarrow MoS_2 + S \quad (14)$$

Raman spectroscopy was further employed to investigate and validate structural and electronic properties of carbon materials [41, 42], as well as the crystal structure of MoS_2 [43, 44]. Figure 2(b) presents the Raman spectra of MoS_2, GO, and MoS_2/C samples. In the Raman spectrum of GO, two prominent bands may be observed. The G band at approximately 1590.5 cm^{-1} corresponds to the sp^2-hybridized carbon network and is attributed to the E_{2g}-symmetry phonon mode of graphitic carbon atoms [41, 42]. The D band at approximately 1346.4 cm^{-1} is assigned to the A_{1g}-symmetry phonons at the K point and is associated with the presence of sp^3-type defects and structural disorder in the carbon framework. The Raman spectrum of the pristine MoS_2 crystal exhibits several characteristic bands in the low-frequency range of approximately 100–550 cm^{-1}. The two intense peaks centered at ~379.1 and ~404.1 cm^{-1} are assigned to the E^1_{2g} and A_{1g} vibrational modes of MoS_2, respectively [44]. In addition, a weak peak observed at approximately 460.3 cm^{-1} is ascribed to the 2LA(M) mode, which corresponds to a second-order Raman scattering process involving longitudinal acoustic phonons at the M point (LA(M)) in the Brillouin zone [45]. These modes correspond exactly to the characteristic structure of the semiconducting 2H-MoS_2 phase. It is the most stable phase of MoS_2 at normal conditions. Generally, the E^1_{2g} mode is associated with the in-plane vibration of Mo and S atoms in opposite directions, whereas the A_{1g} mode corresponds to the out-of-plane vibration of S atoms moving in opposite directions [46], as illustrated in the insets of Figure 2(b). The frequency difference between the A_{1g} and E^1_{2g} modes ($\Delta\omega$) is commonly used to estimate the number of MoS_2 layers [46]. In this study, $\Delta\omega$ is approximately 25 cm^{-1}, which is larger than that of single-layer MoS_2 (~18–19 cm^{-1}) [46, 47] but slightly lower than the typical value for bulk MoS_2 (~26 cm^{-1}) [48–50]. This indicates that the synthesized MoS_2 consists of few-layer structures [51]. In the synthesized nanocomposite, in addition to the peaks at approximately 380.2, 403.6, and 495.0 cm^{-1}, which are assigned to the E^1_{2g}, A_{1g} and $2LA$(M) modes of 2H-MoS_2, respectively, a weak peak at around 230 cm^{-1} is also observed. This peak is attributed to defect-related scattering associated with the longitudinal acoustic (LA(M)) phonon mode at the M point of the Brillouin zone [45, 52]. The peak around ~520 cm^{-1} is due to the Si mode. Interestingly, the calculated intensity ratio (I_D/I_G) of the D and G bands for the MoS_2/C NC is approximately 0.13, which is significantly lower than that of GO ($I_D/I_G \approx 1.55$). This suggests that the in-situ growth of 2D-

MoS_2 nanocrystals on GO sheets during the hydrothermal process may have reduced a substantial number of structural defects and/or partially restored the sp^2-hybridized carbon network in the GO sheets.

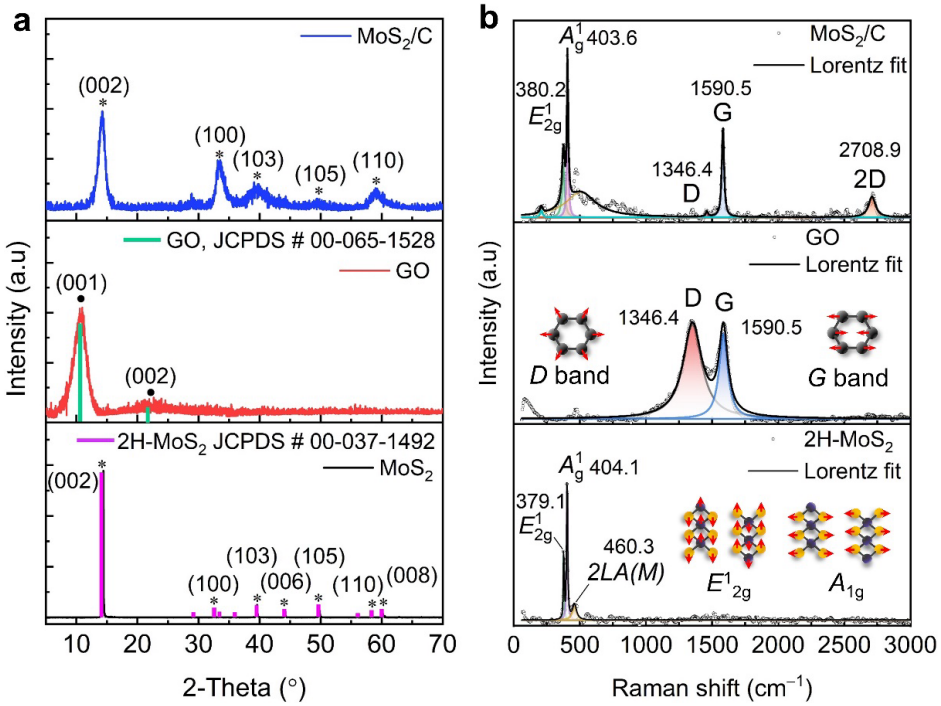

Figure 2. (a) XRD patterns and (b) Raman spectra of GO, 2D-MoS_2 and MoS_2/C NC.

FTIR spectroscopy is an extremely useful tool for identifying different functional groups contained in a sample. Accordingly, FTIR spectroscopy was employed to identify and analyze the functional groups present in GO, MoS_2 and the MoS_2/C NC samples. As shown in Figure 3, the absorbed peaks in range of ~3402–3200 cm^{-1} can be attributed to the −OH bending vibration from the adsorbed H_2O molecules on the surfaces of GO, 2D-MoS_2 and MoS_2/C NC. The peaks located at ~1708 and ~1390 and ~1108 cm^{-1} are due to the C=O stretching vibration of the carbonyl group [53], –OH deformations of C–OH group [54] and C–O–C stretching vibration of epoxide group [55], respectively, existed in the GO nanosheets. As a result, those polar functional groups can provide anchoring sites for the adsorption of MoS_2 on the GO. The characteristic absorption peak at around ~1595–1630 cm^{-1} is attributable to the C=C skeletal vibrations from the unoxidized graphitic domains, confirming the presence of sp^2-hybridized carbon network in the GO nanosheets and MoS_2/C NC [54]. The sharp peak located at ~1406 cm^{-1} is ascribed to the stretching vibration of S–Mo–S [56]. The band centered at ~1120 cm^{-1} is related to the stretching vibration of S–O in MoS_2 nanocrystals [57]. Compared with pristine 2D-MoS_2, a new peak appears at approximately 1020 cm^{-1} in the spectrum of the MoS_2/C NC, which can be attributed to the C=S stretching vibration mode [58]. This observation further suggests the successful incorporation of the 2D-MoS_2 phase within the GO-derived carbon matrix. It has been reported that the interaction between carbon and sulfur—most likely involving unsaturated sulfur species at the edges of 2D-MoS_2 rather than the fully coordinated sulfur atoms within the basal planes—can induce the vertical growth of 2D-MoS_2 nanocrystals on the GO basal plane [59, 60]. The additional peaks at ~910 and ~722 cm^{-1} are assigned to the asymmetric stretching vibration of

Mo=O [61] and asymmetric vibration of the Mo−O groups [62], respectively. A peak at ~667 cm^{-1} is due to characteristic bending vibration of S_xO_y species [63] and/or can be attributed to the S−H stretching vibrations originating as a result of dissociative H_2 adsorption on MoS_2 [64]. In contrast to GO, the disappearance of the C=O and C–O–C peaks in the FTIR spectrum of the MoS_2/C NC indicates that a substantial portion of GO was reduced to rGO during the hydrothermal process. This result is consistent with the XRD analysis, where the characteristic diffraction peaks of GO are no longer observed in the MoS_2/C NC pattern. Combined with the Raman measurements, it was possible to conclude that the MoS_2/C nanocomposites were successfully synthesized.

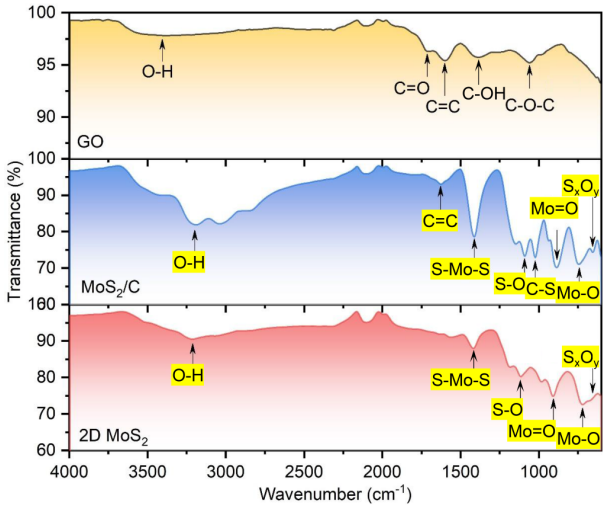

Figure 3. FTIR spectra of GO, 2D-MoS_2, and MoS_2/C NC.

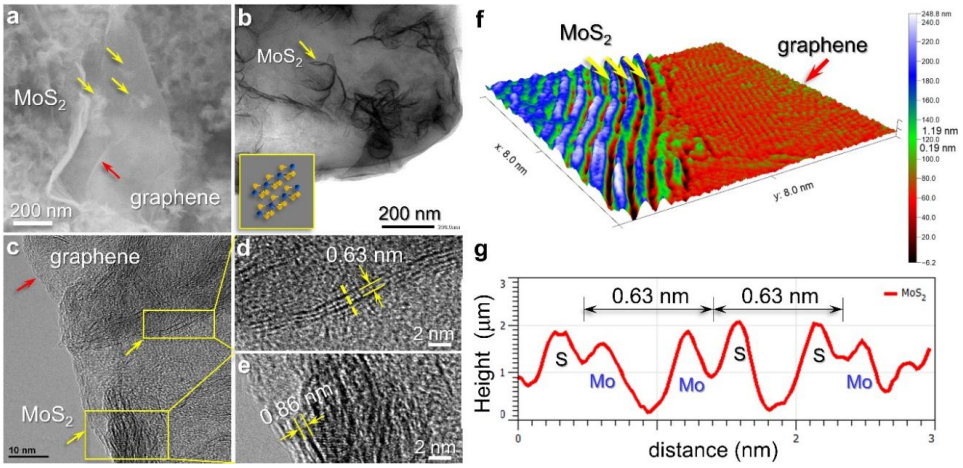

Figure 4. FE-SEM (a), TEM (b), HR-TEM (c-e) images; structural model of the synthesized MoS_2/C NC (f), and (g) extracted surface profile along the yellow dashed line on the HR-TEM image (d).

The surface morphologies and architecture of the synthesized MoS_2/C NC sample can be observed as the composition of ultra-thin 2D-MoS_2 petal-liked sheets (Figure 4(a)) distributing on micron-size GO sheets, with thickness of ~1.8–3.5 nm (~3–6 monolayers) as seen in Figures 4(d) and 4(e). The average lateral sizes of the 2D-MoS_2 petals varies from ~200 to 300 nm (Figure 4(b)). The 3D reconstructed architecture of MoS_2/C NC system in which, the formation

of 2D-MoS_2 crystals on the surfaces and edges of GO nanosheets is depicted in Figure 4(f). The distinct morphological differences highlight the crucial role of the GO matrix as an oriented template that facilitates the in-situ growth of 2D-MoS_2 nanocrystalline structures. The unique layered structure of 2D petal-like MoS_2 crystals is easily distinguishable from the readily visible rGO sheets. These types of morphology were also observed in previous reports [7, 65]. As shown in Figure 4(f), the interlayer spacing of MoS_2 monolayers ranges from approximately 0.63 to 0.86 nm, as determined from the surface profile extracted along the yellow dashed line in Figure 4(d). These values can be indexed to the (002) crystal planes of the 2H-MoS_2 phase. The enlarged $d_{(002)}$ spacing of the MoS_2 crystalline phase indicates that the interlayer distance of the 2D MoS_2 nanopetal-like sheets is significantly expanded compared with the bulk value of 0.615 nm reported in the literature [66]. The formation of the 3D architecture of the MoS_2/C NC can be explained by the self-assembly behavior of graphene, together with partial overlapping and coalescence during the hydrothermal process. During this process, GO is reduced to rGO, as evidenced by the appearance of the 2D band in the Raman spectrum shown in Figure 2(b). The above-mentioned insight analysis shows that the MoS_2/C NC system occupied a vast porous hierarchical and 3D interpenetrating structure, resulting in a large surface area and high electrical conductivity. These structural and morphological features, together with enhanced electrical properties, suggest that the as-synthesized MoS_2/C NC is a promising electrode material for supercapacitor applications. Figure 5(a) presents a representative HAADF-STEM image of the MoS_2/C sample, along with the corresponding EDS elemental mapping images shown in Figures 5(b)–(d). The STEM images and EDS maps clearly demonstrate that MoS_2 is uniformly distributed on the rGO surface without significantly altering the original morphology of the GO sheets. The EDS spectrum of the MoS_2/C sample shown in Figure 5(e) exhibits prominent peaks at approximately 0.277, 2.293, and 2.307 keV, corresponding to the C-Kα, Mo-Kα, and S-Kα signals, respectively. These results confirm the presence of C, Mo, and S elements in the as-synthesized MoS_2/C NC. The elemental composition, summarized in the inset table of Figure 5(e), shows atomic ratios of Mo:C ≈ 1.3:1 and Mo:S ≈ 0.55:1. The calculated atomic ratio of Mo:C in the prepared MoS_2/C NC (≈1.3:1) is slightly lower than the designed ratio (1.5:1), whereas the Mo:S atomic ratio (~1:2) is close to the stoichiometric composition of MoS_2. Thus, the EDS results further corroborate the FE-SEM, TEM/HRTEM, and Raman analyses, confirming the successful synthesis of the nanocomposite via a facile hydrothermal method.

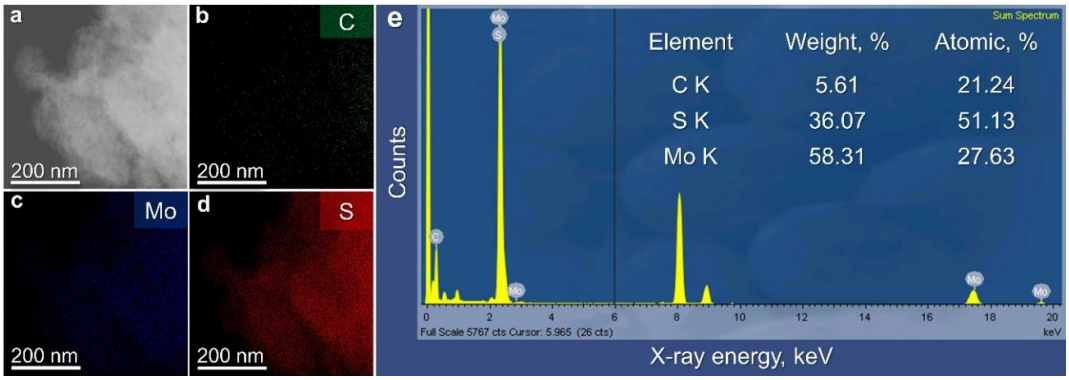

Figure 5. High-angle annular dark-field scanning transmission electron microscopy (HAADF-STEM) image and energy-dispersive X-ray spectroscopy (EDS) elemental mapping images of the MoS_2/C sample: (a) HAADF-STEM image, (b) C, (c) Mo, and (d) S. (e) The EDS spectrum showing the elements and composition present in MoS_2/C NC.

To gain insight into the surface chemical states and elemental composition, XPS measurements were performed on the as-synthesized GO and MoS_2/C samples. The C 1s peak at 284.7 eV was used as a binding energy (BE) reference to correct the XPS spectra for any possible charging effects. Figures 6(a) and 6(b) show the survey-scan XPS spectra of GO and MoS_2/C samples, respectively. In the survey XPS spectrum of GO (Figure 6(a)), two dominant peaks observed at approximately 284.7 and ~532.5 eV are attributed to the C 1s and O 1s core levels, respectively, confirming that carbon and oxygen are the main elements in the GO sheets. For the MoS_2/C sample, four characteristic photoelectron peaks located at approximately 161.7, 230.5, 285.6, and 533.2 eV are assigned to the S 2p, Mo 3d, C 1s, and O 1s core levels, respectively. The S and Mo signals are attributed to the MoS_2 phase, whereas the C and O peaks arise from the presence of GO-derived carbon (rGO) within the composite. These results confirm that MoS_2/C NCs have been prepared successfully via a facile hydrothermal way. No additional peaks associated with impurities are observed in the spectra, indicating the high purity of the synthesized products. A more detailed analysis of the chemical states of S 2p, Mo 3d, C 1s and O 1s was carried out using the narrow-scan of core level XPS spectra.

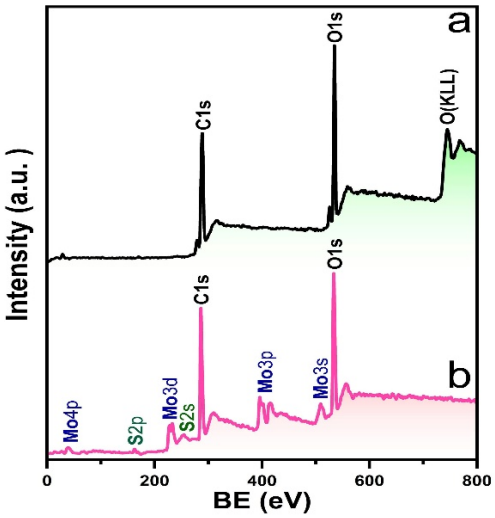

Figure 6. Survey-scan XPS spectra of the as-prepared GO (a) and MoS_2/C NC (b).

Figures 7(a) and (b) present the high-resolution XPS spectra of the C 1s and O 1s regions for the synthesized GO sample, respectively. All spectra were fitted using mixed Gaussian–Lorentzian line shapes after Shirley background subtraction. As shown in Figure 7(a), the high-resolution C 1s spectrum can be deconvoluted into six distinct components. The peaks located at approximately 284.7, 285.7, 286.1, 288.3, 288.9, and 290.4 eV are assigned to the C=C/C–C, C–OH, C–O–C, C=O, COOH, and π–π* functional groups, respectively [67]. Figure 7(b) presents the high-resolution O 1s spectrum, which can be deconvoluted into four components. The two dominant peaks at approximately 532.4 and 533.9 eV are assigned to C–O–C and C–O bonds, respectively, while two weaker peaks at around 531.1 and 535.6 eV correspond to C=O and C–OH groups, respectively. Figures 7(c)-(f) present the high-resolution XPS spectra of the C 1s, S 2p, Mo 3d, and O 1s regions for the synthesized MoS_2/C sample, respectively. As shown in Figure 7(c), the C 1s spectrum can be deconvoluted into six distinct components. The peaks located at approximately 285.0, 285.7, 286.5, 288.1, 288.8, and 290.0 eV are assigned to the C=C/C–C, C–OH, C–O–C, C=O, COOH, and π–π* functional groups, respectively. This result suggests that some oxygen-containing functional groups remain on the rGO surface, indicating that the

reduction of GO was not complete. The high-resolution O 1s spectrum in Figure 7(d) can be deconvoluted into six distinct components at approximately 530.8, 531.9, 533.0, 534.0, 536.0, and 537.2 eV. These peaks are assigned to C=O, C–O–C, C–O, Mo–O/S–O species in MoS_xO_y (arising from slight surface oxidation of MoS_2 upon air exposure) [68, 69], C–OH groups, and adsorbed H_2O, respectively. As shown in Figure 7(e), the high-resolution S 2p XPS spectrum can be deconvoluted into six distinct peaks. The peaks at approximately 161.5 and 163.4 eV are assigned to S^{2-} $p_{3/2}$ and S^{2-} $p_{1/2}$ states in metallic 1T-MoS_2, respectively [70]. The doublet peaks located at around 162.5 and 164.7 eV correspond to S^{2-} $p_{3/2}$ and S^{2-} $p_{1/2}$ in semiconducting 2H-MoS_2, respectively [71, 72]. In addition, minor peaks at approximately 168.7 and 169.8 eV are attributed to oxidized sulfur species, such as sulfate, sulfite, and/or thiosulfate groups [73]. As shown in Figure 7(f), the high-resolution Mo 3d XPS spectrum can be deconvoluted into seven components centered at approximately 226.5, 228.7, 229.8, 231.8, 232.8, 234.8, and 236.9 eV. The peak at ~226.5 eV is attributed to the S 2s signal [74]. The doublet at ~229.8 and ~232.8 eV corresponds to Mo^{4+} $3d_{5/2}$ and Mo^{4+} $3d_{3/2}$ states in semiconducting 2H-MoS_2 [75], while the peaks at ~228.7 and ~231.8 eV, shifted to lower binding energies by ~1.0 eV, are assigned to Mo^{4+} $3d_{5/2}$ and Mo^{4+} $3d_{3/2}$ in metallic 1T-MoS_2 [76]. The remaining peaks at ~234.8 and ~236.9 eV are attributed to Mo^{+6} $3d_{5/2}$ [77] and Mo^{6+} $3d_{3/2}$ states associated with MoS_xO_y species [78], likely arising from slight surface oxidation of MoS_2 upon exposure to air after synthesis and washing, prior to XPS measurement.

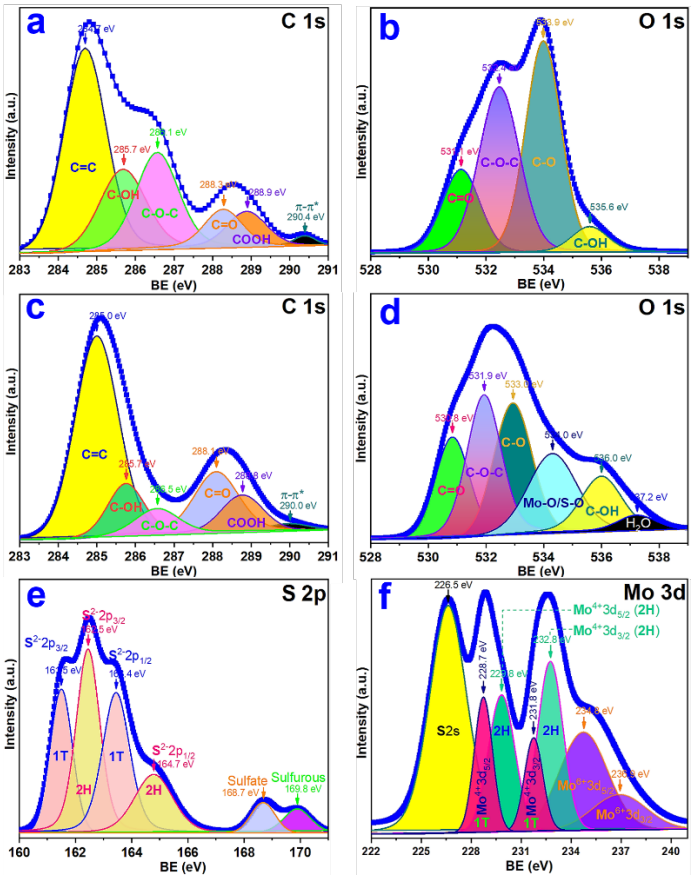

Figure 7. High-resolution XPS spectra of GO: a) C 1s and b) O 1s regions; high-resolution XPS spectra of MoS_2/C NC: c) C 1s, d) O 1s, e) S 2p, and f) Mo 3d regions.

3.2. Specific capacitance and electrochemical properties of MoS_2/C NC

The electrochemical properties of the synthesized MoS_2/C NC were evaluated using cyclic voltammetry (CV) and electrochemical impedance spectroscopy (EIS) in a three-electrode configuration with 3 M KCl as the electrolyte. The working electrodes (GO, 2D-MoS_2 and MoS_2/C NC materials) were fabricated by coating with ~0.1 mg paste of MoS_2/C NC (93 % MoS_2/C NC and 6.0 % black carbon), GO and bare 2D-MoS2, respectively. The CV curves of the fabricated electrodes were recorded at scan rates ranging from 5 to 100 mV s^{-1}, as shown in Figure 8. Observing the CV curve of MoS_2/C NC electrode and areas under the curves in Figure 8(a), it is clear to see that the MoS_2/C NC electrode exhibits higher specific capacitance (C_{sp}) than those of prepared GO and 2D-MoS_2 electrodes. Noteworthily, the CV curve of the MoS_2/C NC approaches a rectangular-type shape of an ideal capacitor within the operating potential window between −1.1 and 0.1 V (vs. Ag/AgCl). Specifically, the MoS_2/C NC working electrode exhibits a specific capacitance of approximately 118.3 F g^{-1} at a scan rate of 30 mV s^{-1}, which is about 390 times higher than that of GO-coated electrode (~0.3 F g^{-1}) and approximately 23 times greater than that of the 2D-MoS_2 electrode (~5.3 F g^{-1}). Furthermore, the fabricated MoS_2/C NC electrode shows improved energy density which approaches E ~87.98 Wh kg^{-1} and P ~366.6 W kg^{-1}, respectively.

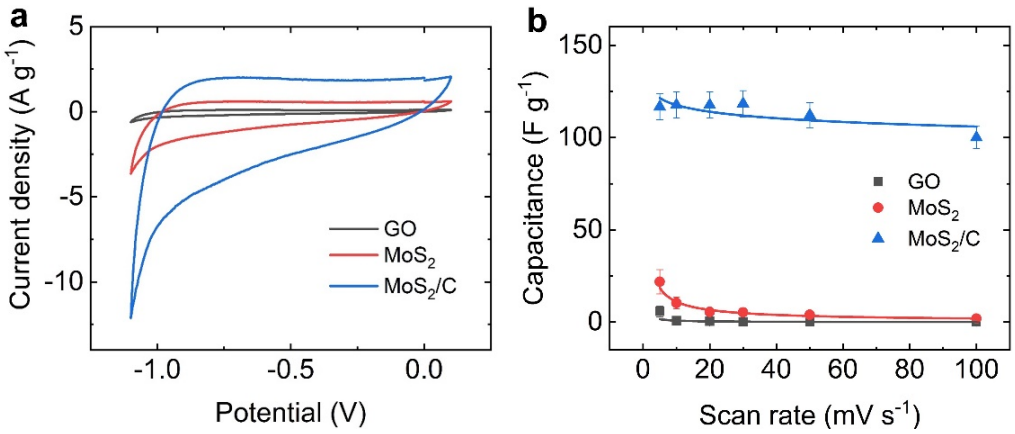

Figure 8. a) CV curves and b) specific capacitances of the fabricated GO, 2D-MoS2 and MoS_2/C NC electrodes.

The enhanced specific capacitance and energy density of the MoS_2/C NC, compared with GO and 2D MoS_2, can be attributed to its unique and robust composite architecture, which can be explained by two key factors. First, the formation of a highly porous 3D network (Figure 4) arises from the growth of 2D MoS_2 nanostructures on the surfaces and edges of rGO sheets. XRD analysis shows that the interlayer spacing $d_{(002)}$, calculated using Bragg's equation, is approximately 0.63 nm, which is favorable for the rapid intercalation of hydrated $(H_2O)_6Na^+$ ions (radius ~2.43 Å) [79] into the MoS_2 layers. This porous 3D architecture facilitates efficient transport and diffusion of charge carriers, including electrons and electrolyte ions, along shortened pathways to the electrode–electrolyte interface during the charging and discharging processes. The rGO matrix in the synthesized MoS_2/C NC system serves not only as a suitable substrate for the growth and uniform dispersion of 2D MoS_2 nanocrystals—thereby increasing the specific surface area—but also as a highly conductive network that facilitates rapid charge transport. The specific capacitance and overall electrochemical performance of the capacitor

electrodes fabricated from MoS_2/C NC, GO, and 2D MoS_2 were evaluated as a function of scan rate and are summarized in Tables 1 and 2.

Table 1. Specific capacitance of MoS_2/C, GO, and 2D-MoS_2 electrodes.

Scan rate, mV s^{-1}	Specific capacitance, F g^{-1}		
	GO	MoS_2/C	2D-MoS_2
5	5.8	116.7	21.9
10	0.8	117.7	10.4
20	0.4	117.7	5.5
30	0.3	118.5	5.3
50	0.2	112.1	4.0
100	0.1	100.0	1.9

Table 2. Electrochemical performance of MoS_2/C, GO, and 2D-MoS_2 electrodes at the scan rate of 30 mV s^{-1}.

Electrode(s)	Potential window, V	C_{sp}, F g^{-1}	E, Wh kg^{-1}	P, W kg^{-1}
MoS_2/C	1.2	118.5	88.0	367.0
GO	1.2	0.3	0.6	0.009
2D-MoS2	1.2	5.3	10.6	0.155

As seen in Table 3, when comparing with the reported specific capacitance of MoS_2 @ 3D porous graphene (~63.8 F g^{-1}) obtained by Zhang *et al.* [80], or MoS_2 nanospheres (~112 F g^{-1}) synthesized by Kumar *et al.* [67], the specific capacitance of the as-synthesized MoS_2/C NC in this work is quite high (~118.5 F g^{-1}) over operating potential window (~ 0 ÷ -1.2 V). Our findings are mostly comparable to the previous reports [81-83], for a variety of similar composite electrode materials, demonstrating the remarkable capacitive behavior of the synthesized MoS_2/C NC [84]. These results suggest that the hydrothermal method employed in this work is more effective for synthesizing MoS_2/C NC with short reaction time as well as enabling control over the crystallite size and morphology of the synthesized MoS_2/C NC, contributing to its high specific capacitance and excellent electrochemical properties.

Table 3. Comparison of specific capacitance with reported literatures.

Aqueous electrolyte	Electrode material	Device configuration	Voltage V	C_{sp} F g^{-1}	E_{sp} Wh kg^{-1}	P_{max} W kg^{-1}	Ref.
1 M Na_2SO_4	MoS_2/C NC	3-Electrode	-1.2	118.5	88.0	367.0	This work
1 M KCl	MoS_2 nanospheres	3-Electrode	-0.9	112.0	-	-	[65]
1 M $LiPF_6$	MoS_2 @ 3D porous graphene	2-Electrode	4.0	63.8	97	8314	[80]
1 M Na_2SO_4	MoS_2/C nanosheets	3-Electrode	-0.6	108.0	7.40	3700	[81]
0.1 M Na_2SO_4	RGO	3-Electrode	-0.8	41.0	-	-	[82]
3 M KOH	C/MoS_2	3-Electrode	0.5	210.0	-	-	[83]

Electrochemical impedance spectroscopy is a powerful technique widely used to analyze material structure and the kinetic processes occurring at the electrode–electrolyte interface, thereby providing insight into the underlying charge storage mechanisms in the MoS_2/C NC electrode system. The impedance measurements were conducted on the fabricated MoS_2/C NC, GO, and 2D-MoS_2 electrodes over a frequency range of 10 mHz to 100 kHz within an open-circuit potential window of −1.2 to 0.2 V, with an alternating voltage amplitude of 10 mV (Figures 9(a)–(c), (d)). The complex impedance $Z(\omega)$ of the synthesized MoS_2/C NC were modeled and presented as Nyquist plot (Z' vs. $-Z$"), and Bode plot, in which $Z'(\omega)$ and $Z''(\omega)$ are the real and the imaginary part, respectively, of the impedance. The Nyquist plots of the synthesized GO, 2D MoS_2, and MoS_2/C NC samples (Figures 9(a) and (c)) exhibit two distinct regions, consisting of a semicircle in the HF region and a linear segment in the low-frequency (LF) region. Based on the Nyquist plot data, the electrode-electrolyte interface can be modeled by an equivalent circuit (Figure 9(e)) in which the equivalent series resistance R_S (Ω cm^2) is composed of ionic resistance of the electrolyte, intrinsic resistance of MoS_2/C NC, and the contact resistance at the interface between the MoS_2/C NC electrode material and the current collector. The R_{CT} (Ω cm^2) is the faradaic charge transfer resistance, W (S s$^{-1/2}$ cm^{-2}) is the Warburg impedance associated with ionic diffusion in the electrolyte, and C_{dl} (F cm^{-2}) is the double layer capacitance.

Electrochemical fitted parameters of the electrodes fabricated from MoS_2/C NC, GO, and 2D-MoS_2 are summarized in Table 4. It is noticed that the fabricated MoS_2/C NC electrode possesses small values of resistance R_S and R_{CT} when compared with that of GO and 2D-MoS_2 electrodes. It can be seen that in the HF region, the intrinsic resistance R_{CT} of GO electrode is ~2.616 Ω cm^{-2} while the MoS_2/C NC is ~22.610 Ω cm^{-2}, which is much lower than that of 2D-MoS_2 alone (~72.550 Ω cm^{-2}), indicated by the radius of the corresponding semi-circles in Figure 9(c). The low resistance values are beneficial, and responsible for enhancement of electrical transport property such as fast charge transfer and ion diffusion, thereby enhancing electrochemical property of the synthesized MoS_2/C NC electrode material.

Table 4. Electrochemical parameters calculated for MoS_2/C NC, GO, and 2D-MoS_2 electrodes.

Electrode materials	R_S (Ω cm^2)	R_{CT} (Ω cm^2)	C_{dl} (mF cm^2)	W (S s$^{-1/2}$ cm^{-2})	S_E (m^2 g^{-1})	τ_o (ms)
MoS_2/C NC	25.680	22.610	23.550	0.0028	217.6	159.1
2D-MoS_2	26.170	72.550	0.752	0.0012	124.5	0.032
GO	27.310	2.616	9.086 10^{-3}	0.0016	161.7	0.025

The complex capacitance model was further analyzed to examine the relationship between the specific capacitance of the as-fabricated MoS_2/C NC electrode and the applied frequency, as shown in Figures 9(b) and 9(d). The Bode plots in Figures 9(b) and 9(d) show the frequency responses of the electrode materials under the applied frequency. In this model, the cell capacitance is expressed in terms of its real and imaginary components, as defined in Eqs. (5) and (6). Compared with GO and 2D-MoS_2 electrodes, the MoS_2/C NC electrode system shows a considerably low in frequency response with large phase angle ($-\phi$, °), which is a characteristic of good capacitive performance and large energy storage capability. The response frequency of MoS_2/C NC electrode (~1.0 Hz) is significantly lower than those of 2D-MoS_2 (~5012 Hz) and GO electrodes (~6309 Hz). Furthermore, the relaxation time τ (s) calculated from the knee frequency f_o, (Hz) corresponding to the maximum of $-Z''(\omega)$ in the Nyquist Plot (LF region) was used to evaluate the electrochemical capacitance properties and charge–discharge characteristic response. The τ values obtained for the MoS_2/C NC, GO and bare 2D-MoS_2 electrodes are about

~159.1, 0.025 and 0.032 ms, respectively. The relaxation time of the MoS_2/C NC electrode to be significantly higher than that of GO and bare 2D-MoS_2, indicating the low-discharge characteristic response and good electrochemical capacitive storage. In addition, the charge conductivity of MoS_2/C NC electrode also increases significantly compared with that of 2D-MoS_2 due to the presence of rGO matrix in the MoS_2/C NC.

The electrochemically active surface area S_E ($m^2\ g^{-1}$) of the fabricated MoS_2/C NC electrode was calculated using Eq. (7) to be approximately 218.0 $m^2\ g^{-1}$, which is higher than that of GO (~161.7 $m^2\ g^{-1}$) and bare 2D MoS_2 (~124.5 $m^2\ g^{-1}$) electrodes. These results are consistent with previous reports [84]. The large active surface area of the MoS_2/C NC implies that the 2D-MoS_2 nanostructure growing and well dispersing in the GO matrix and resulting in rich porous composite architecture as previously observed by TEM and HR-TEM images in Figure 4.

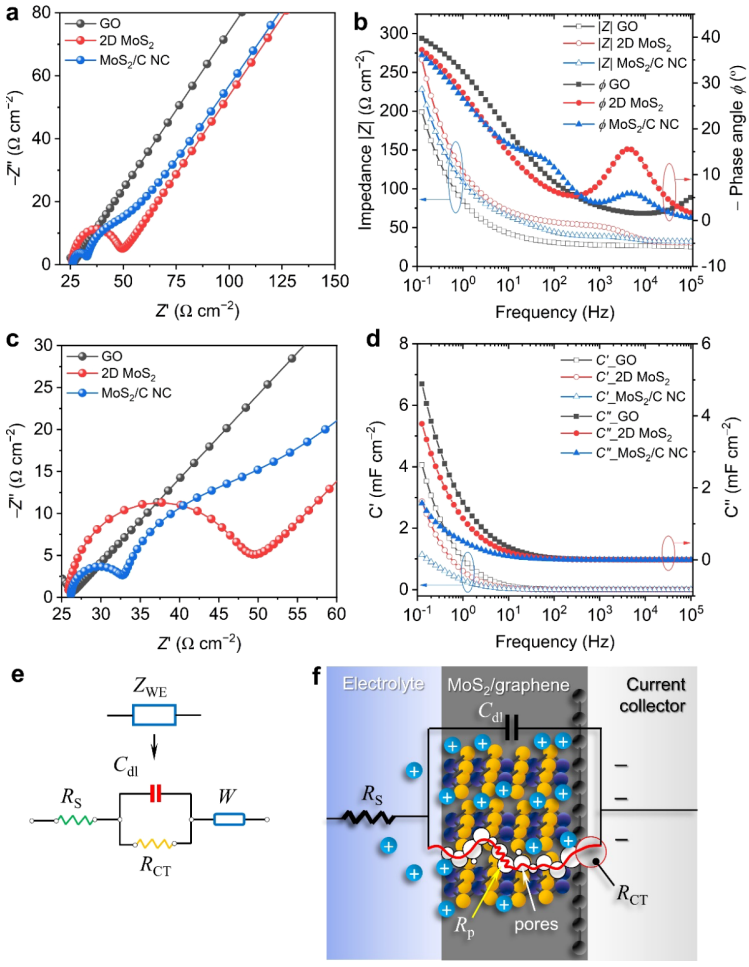

Figure 9. Electrochemical impedance of MoS_2/C NC, GO, and 2D-MoS_2 electrodes. (a) Nyquist plot, (b) Bode plot, (c) Magnified view of (a) in the high frequency region, and (d) capacitances with respect to frequencies. (e) Equivalent circuit modeling the electrolyte-electrode interface. (f) Schematic diagram showing the electric double layer and intercalation of ions between 2D-MoS_2 layers.

The capacitive energy storage mechanism of the electrode material can be described as the accumulation of charge at the electrolyte-electrode interface. The enhanced capacitive energy storage observed for the MoS_2/C NC electrode can be attributed to the combined contributions of

electric double-layer capacitance and Faradaic (redox) reactions, along with the increased electrochemically active surface area resulted from the reduced number of MoS_2 layers grown on GO sheets during the hydrothermal process. First, ions accumulate at the interface of the electric double layer between MoS_2 nanocrystalline sheets and the electrolyte as illustrated in Figure 9(f). Then, during charging, alkali ions from the electrolyte (Na^+ in this case) adsorb on the surfaces and intercalate between 2D-MoS_2 layers (reduction reaction), followed by discharging and deintercalation of the ions (oxidation reaction) as represented by faradaic (Eq. (15)) and non-faradaic (Eq. (16)) mechanism [85, 86]:

$$MoS_2 + yNa^+ + ye^- \leftrightarrow Na_yMoS_2 \quad (15)$$

$$(MoS_2)_{surface} + yNa^+ \leftrightarrow (Na^+ - MoS_2^-)_{surface} \quad (16)$$

It is evident that the electric double-layer capacitance originates from the rGO matrix, whereas the pseudocapacitance arises from surface redox reactions of the 2D MoS_2 phase dispersed within the rGO framework. The presence of rGO matrix in the MoS_2/C NC provides a high electronic conductive platform and large specific surface area for growing 2D-MoS_2 nanostructures. In addition, the intercalation of large ions from the electrolyte to the vdW gaps between MoS_2 layers prevented them from aggregation. The repeated intercalation – deintercalation of the ions and charged carriers during multiple charging/discharging process could enlarge the MoS_2 intra-layer gaps and even exfoliate 2D-MoS_2 monolayers. This process leads to an increase in the overall specific surface area, thereby improving the specific capacitance of the MoS_2/C NC electrode system.

4. CONCLUSIONS

Low-dimensional MoS_2/C nanocomposites with a 3D porous architecture were successfully synthesized via the in-situ growth of 2D-MoS_2 nanocrystals within a GO matrix using a facile one-pot hydrothermal method. The morphology, phase structure, chemical composition, and electrochemical properties of the as-prepared materials were systematically characterized by FE-SEM, HR-TEM, XRD, EDS, XPS, FTIR, Raman spectroscopy, and electrochemical techniques. The results demonstrate that the 2H-MoS_2 nanocrystals exhibit a petal-like morphology with a thickness of approximately 1.8–3.5 nm and an average lateral size of 200–300 nm and are uniformly distributed across the rGO nanosheets. Electrochemical measurements indicate that the MoS_2/C NC delivers a specific capacitance of ~118.5 F g^{-1}, an energy density of ~88.0 Wh kg^{-1}, and a power density of ~367.0 W kg^{-1}, along with a high specific surface area of ~218.0 m^2 g^{-1}. The enhanced electrochemical performance can be attributed to the ultrathin nature of the 2D MoS_2 nanocrystals and the synergistic interaction between the dispersed MoS_2 phase and the conductive rGO matrix, which together facilitates efficient charge storage and transport. These findings suggest that the synthesized MoS_2/C NC is a promising electrode material for supercapacitor applications in microelectronic devices.

Acknowledgments. This research is funded by Vietnam National Foundation for Science and Technology Development (NAFOSTED) under Grant No. 104.03-2019.42. We acknowledge the support of time and facilities from Ho Chi Minh City University of Technology (HCMUT), VNU-HCM for supporting this study.

CRediT authorship contribution statement. Le Ngoc Long: Investigation, Methodology, Visualization, Writing – original draft. Tran Van Khai: Conceptualization, Data curation, Formal analysis, Resources, Supervision, Validation, Writing – review & editing.

Declaration of competing interest. The authors declare that they have no known competing financial interests or personal relationships that could have appeared to influence the work reported in this paper.

REFERENCES

1. Conway B. E. - Electrochemical supercapacitors: Scientific fundamentals and technological applications, New York: Plenum (1999).
2. Miller J. R., Simon P. - Electrochemical capacitors for energy management. Science, **321**(5889) (2008) 651-652. https://doi.org/10.1126/science.1158736.
3. Geim A. K. - Nobel Lecture: Random walk to graphene. Rev. Mod. Phys., **83**(3) (2011) 851-862. https://doi.org/10.1103/RevModPhys.83.851.
4. Novoselov K. S., Geim A. K., Morozov S. V., Jiang D., Zhang Y., Dubonos S. V., Grigorieva I. V., Firsov A. A. - Electric field effect in atomically thin carbon films. Science, **306** (2004) 666-669. https://doi.org/10.1126/science.1102896.
5. Castro Neto A. H., Guinea F., Peres N. M. R., Novoselov K. S. and Geim A. K. - The electronic properties of graphene. Rev. Mod. Phys., **81** (2009) 109-162. https://doi.org/10.1103/RevModPhys.81.109.
6. Abergel D. S. L., Apalkov V., Berashevich J., Ziegler K., Chakraborty T. - Properties of graphene: A theoretical perspective. Adv. Phys., **59** (2010) 261-482. https://doi.org/10.1080/00018732.2010.487978.
7. Huang K. J., Wang L., Liu Y. J., Liu Y. M., Wang H. B., Gan T. and Wang L. L. - Layered MoS_2-graphene composites for supercapacitor applications with enhanced capacitive performance. Int. J. Hydrog. Energy, **38** (2013) 14027-14034. https://doi.org/10.1016/j.ijhydene.2013.08.112.
8. David L., Bhandavat R. and Singh G. - MoS_2/graphene composite paper for sodium-ion battery electrodes. ACS Nano, **8** (2014) 1759-1770. https://doi.org/10.1021/nn406156b.
9. Ma L., Huang G., Chen W., Wang Z., Ye J., Haiyang L., Chen D. N. S., Lee J. Y. - Cationic surfactant-assisted hydrothermal synthesis of few-layer molybdenum disulfide/graphene composites: Microstructure and electrochemical lithium storage. J. Power Sources, **264** (2014) 262-271. https://doi.org/10.1016/j.jpowsour.2014.04.084.
10. Peng X., Peng L., Wu C., Xie Y. - Two dimensional nanomaterials for flexible supercapacitors. Chem. Soc. Rev., **43** (2014) 3303-3323. https://doi.org/10.1039/c3cs60407a.
11. Mak K. F., Lee C., Hone J., Shan J., Heinz T. F. - Atomically thin MoS_2: A new direct-gap semiconductor. Phys. Rev. Lett., **105** (2010) 136805-136808. https://doi.org/10.1103/PhysRevLett.105.136805.
12. Kuc A. - Low-dimensional transition-metal dichalcogenides. Chem. Model., **11** (2014) 1-29. https://doi.org/10.1039/9781782620112-00001.
13. Novoselov K. S., Jiang D., Schedin F., Booth T. J., Khotkevich V. V., Morozov S. V., Geim A. K. - Two-dimensional atomic crystals. Proc. Natl. Acad. Sci. U.S.A., **102** (2005) 10451-10453. https://doi.org/10.1073/pnas.0502848102.
14. Li X., Guo S., Li W., Ren X., Su J., Song Q., Sobrido A. J., Wei B. - Edge-Rich MoS_2 Grown on Edge-Oriented Three-Dimensional Graphene Glass for High-Performance Hydrogen Evolution. Nano Energy, **57** (2019) 388-397. https://doi.org/10.1016/j.nanoen.2018.12.044.
15. Yadav V., Roy S., Singh P., Khan Z., Jaiswal A. - 2D MoS_2-Based Nanomaterials for Therapeutic, Bioimaging, and Biosensing Applications. Small, **15** (2019) 1803706. https://doi.org/10.1002/smll.201803706.
16. Britnell L., Ribeiro R. M., Eckmann A., Jalil R., Belle B. D., Mishchenko A., Kim Y. J., Gorbachev R. V., Georgiou T., Morozov S. V., Grigorenko A. N., Geim A. K., Casiraghi C., Castro-Neto A. H., Novoselov K. S. - Strong light-matter interactions in heterostructures of atomically thin films. Science, **340**(6138) (2013) 1311-1314. https://doi.org/10.1126/science.1235547.
17. Long L. N., Kien P. T., Khai T. V. - Synthesis of MoS_2/graphene nanocomposite by facile ultrasonic-assisted hydrothermal method. Vietnam J. Sci. Technol., **57** (2019) 703-713. https://doi.org/10.15625/2525-2518/57/6/13955.

18. Xuan T. T., Long L. N., Khai T. V. - Effect of reaction temperature and reaction time on the structure and properties of MoS_2 synthesized by hydrothermal method. Vietnam J. Chem., **58** (2020) 92-100. https://doi.org/10.1002/vjch.2019000144.
19. Long L. N., Quang N. T., Khuong T. T., Kien P. T., Thang N. H. , Khai T. V. - Controllable synthesis by hydrothermal method and optical properties of 2D MoS_2/rGO nanocomposites, *J. Sol-Gel Sci. Technol*., **106** (2023) 699-714. https://doi.org/10.1007/s10971-023-06072-3.
20. Khai T. V., Long L. N., Phong M. T., Kien P. T., Thang L. V., Lam T. D. - Synthesis and optical properties of MoS_2/graphene nanocomposite. J. Electron. Mater., **49** (2020) 969-979. https://doi.org/10.1007/s11664-019-07670-0.
21. Sirat M. S., Johari M. H., Mohmad A. R., Shazni M. A., Haniff M., Ani M. H., Hussin M. R. M., Mohamed M. A. - Direct growth and properties of few-layer MoS_2 on multilayer graphene prepared by chemical vapor deposition. J. Mater. Sci., **57** (2022) 19704-19715. https://doi.org/10.1007/s10853-022-07873-7.
22. Shi Y., Zhou W., Lu A.Y., Fang W., Lee Y. H., Hsu A.L., Kim S. M., Kim K. K., Yang H. Y., Li L. J., Idrobo J. C., Kong J. - van der Waals epitaxy of MoS_2 layers using graphene as growth templates. Nano Lett., **12** (2012) 2784-2791. https://doi.org/10.1021/nl204562j.
23. Kumar D. P., Hong S., Reddy D. A., Kim T. K. - Ultrathin MoS_2 layers anchored exfoliated reduced graphene oxide nanosheet hybrid as a highly efficient cocatalyst for CdS nanorods towards enhanced photocatalytic hydrogen production. Appl. Catal., B **212** (2017) 7-14. https://doi.org/10.1016/j.apcatb.2017.04.065.
24. Fu M., Zhu Z., Chen W., Yu H., Liu Q. - Microwave-assisted synthesis of MoS_2/graphene composites for supercapacitors, J. Mater. Sci., **55** (2020) 16385-16393. https://doi.org/10.1007/s10853-020-05201-5.
25. Kandhasamy D. M., Mareeswaran P. M., Chellappan S., Namasivayam D., Aldahish A., Chidambaram K. - Synthesis and photoluminescence properties of MoS_2/graphene heterostructure by liquid-phase exfoliation. ACS Omega, **7** (2022) 629-637. https://doi.org/10.1021/acsomega.1c05250.
26. Hummers W.S., Offeman R. E. - Preparation of graphitic oxide. J. Am. Chem. Soc., **80**(6) (1958) 1339. https://doi.org/10.1021/ja01539a017.
27. Khai T. V., Lam T. D., Thu L. V., Kim H. W. - A two-step method for the preparation of highly conductive graphene film and its gas-sensing property. Mater. Sci. Appl., **6** (2015) 963-977. https://doi.org/10.4236/msa.2015.611097.
28. Khai T. V., Long L. N., Khoi N. H. T., Thang N. H. - Effects of hydrothermal reaction time on the structure and optical properties of ZnO/graphene oxide nanocomposites. *Crystals*, **12**(12) (2022) 1825. https://doi.org/10.3390/cryst12121825.
29. Khai T. V., Kwak D. S., Kwon Y. J., Kim S. S., Shim K. B., Kim H. W. - High-quality graphene thin films synthesized by H_2 ambient-annealing of reduced graphene oxide sheets. J. Ceram. Process Res., **14** (2013) 355-362.
30. Hamelin A., Vitanov T., Sevastyanov E., Popov A. - The electrochemical double layer on sp metal single crystals: the current status of data. J. Electroanal. Chem. Interfacial Electrochem., **145** (1983) 225-264. https://doi.org/10.1016/S0022-0728(83)80085-0.
31. Pech D., Brunet M., Durou H., Huang P., Mochalin V., Gogotsi Y., Taberna P. L., Simon P. - Ultrahigh-power micrometre-sized supercapacitors based on onion-like carbon. Nat. Nanotechnol., **5** (2010) 651-654. https://doi.org/10.1038/nnano.2010.162.
32. Gund G. S., Dubal D. P., Patil B. H., Shinde S. S., Lokhande C. D. - Enhanced activity of chemically synthesized hybrid graphene oxide/Mn_3O_4 composite for high performance supercapacitors. Electrochim. Acta, **92** (2013) 205-215. https://doi.org/10.1016/j.electacta.2012.12.120.
33. Cullity B. D., Stock S.R. - Elements of X-ray Diffraction, in Diffraction I: The directions of diffracted beams, N.J, Upper Saddle River: Pearson (2001).
34. Yunus R. M., Endo H., Tsuji M., Ago H., Vertical heterostructures of MoS_2 and graphene nanoribbons grown by two-step chemical vapor deposition for high-gain photodetectors. Phys. Chem. Chem. Phys., **17** (2015) 25210-25215. https://doi.org/10.1039/C5CP03958D.

35. Zhao B., Wang Z., Gao Y, Chen L., Lu M., Jiao Z., Jiang Y., Ding Y., Cheng L. - Hydrothermal synthesis of layer-controlled MoS_2/graphene composite aerogels for lithium-ion battery anode materials. Appl. Surf. Sci., **390** (2016) 209-215. https://doi.org/10.1016/j.apsusc.2016.08.078.
36. Fei L., Lei S., Zhang W. B., Lu W., Lin Z., Lam C. H., Chai Y., Yu W., - Direct TEM observations of growth mechanisms of two-dimensional MoS_2 flakes. Nat. Commun., **7** (2016) 12206. https://doi.org/10.1038/ncomms12206.
37. Yang L., Cui X., Zhang J., Wang K., Shen M., Zeng S., Dayeh S. A., Feng L., Xiang B. - Lattice strain effects on the optical properties of MoS_2 nanosheets, Sci. Rep., **4** (2014) 5649. https://doi.org/10.1038/srep05649.
38. Nethravathi C., Rajamathi M. - Chemically modified graphene sheets produced by the solvothermal reduction of colloidal dispersions of graphite oxide. Carbon, **46** (2008) 1994-1998. https://doi.org/10.1016/j.carbon.2008.08.013.
39. Zou L., Qu R., Gao H., Guan X., Qi X., Liu C., Zhang Z., Lei X., - MoS_2/RGO hybrids prepared by a hydrothermal route as a highly efficient catalytic for sonocatalytic degradation of methylene blue. Results Phys., **14** (2019) 102458. https://doi.org/10.1016/j.rinp.2019.102458.
40. Long L. N., Thi P. T., Trung P. T., Kien P. T., Ohtani M., Kumabe Y., Tanaka H., Ueda S., Lee H., ThangP. B., Khai T. V. - Controllable synthesis of MoS_2/graphene low-dimensional nanocomposites and their electrical properties. Appl. Surf. Sci., **504** (2020) 144193. https://doi.org/10.1016/j.apsusc.2019.144193.
41. Bokobza L., Bruneel J. L., Couzi M. - Raman spectroscopy as a tool for the analysis of carbon-based materials (highly oriented pyrolitic graphite, multilayer graphene and multiwall carbon nanotubes) and of some of their elastomeric composites. Vib. Spectrosc., **74** (2014) 57-63. https://doi.org/10.1016/j.vibspec.2014.07.009.
42. Ferrari A. C., Basko D. M. - Raman spectroscopy as a versatile tool for studying the properties of graphene. Nat. Nanotechnol., **8** (2013) 235-246. https://doi.org/10.1038/nnano.2013.46.
43. Buscema M., Steele G. A., van der Zant H. S. J, Castellanos-Gomez A. - The effect of the substrate on the Raman and photoluminescence emission of single-layer MoS_2. Nano Res., **7** (2014) 561-571. https://doi.org/10.1007/s12274-014-0424-0.
44. Gołasa K., Grzeszczyk M., Bożek R., Leszczyński P., Wysmołek A., Potemski M., Babinski A. - Resonant Raman scattering in MoS_2-From bulk to monolayer. Solid State Commun., **197** (2014) 53-56. https://doi.org/10.1016/j.ssc.2014.08.009.
45. Mignuzzi S., Pollard A. J., Bonini N., Brennan B., Gilmore I. S., Pimenta M. A., Richards D., Roy D. - Effect of disorder on Raman scattering of single-layer MoS_2, Phys. Rev. B, **91** (2015) 195411. https://doi.org/10.1103/PhysRevB.91.195411.
46. Lee C., Yan H., Brus L. E., Heinz T. F., Hone J., Ryu S., Anomalous Lattice Vibrations of Single-and Few-Layer MoS_2. ACS Nano, **4** (2010) 2695-2700. https://doi.org/10.1021/nn1003937.
47. Molina-Sánchez A., Wirtz L. - Phonons in single-layer and few-layer MoS_2 and WS_2. Phys. Rev. B, **84** (2011) 155413. https://doi.org/10.1103/PhysRevB.84.155413.
48. Liu Y. J., Hao L. Z., Gao W., Liu Y. M., Li G. X., Xue Q. Z., Guo W. Y., Yu L. Q., Wu Z. P., Liu X. H., Zeng H. Z., Zhu J. - Growth and humidity-dependent electrical properties of bulk-like MoS_2 thin films on Si, RSC Adv., **5** (2015) 74329-74335. https://doi.org/10.1039/C5RA11454C.
49. Chakraborty B., Matte H. S. S. R., Sood A. K. and Rao C. N. R. - Layer-dependent resonant Raman scattering of a few layer MoS_2, J. Raman Spectrosc., **44** (2013) 92-96. https://doi.org/10.1002/jrs.4147.
50. Ganatra R., Zhang Q. - Few-layer MoS_2: a promising layered semiconductor. ACS Nano, **8** (2014) 4074-4099. https://doi.org/10.1021/nn405938z.
51. Hussain S., Shehzad M. A., Vikraman D., Khan M. F., Singh J., Choi D., Seo Y., Eom J., Lee W., Jung J. - Synthesis and characterization of large-area and continuous MoS_2 atomic layers by RF magnetron sputtering. Nanoscale, **8** (2016) 4340-4347. https://doi.org/10.1039/C5NR09032F.
52. Zhang X., Qiao X., Shi W., Wu J., Jiang D., Tan P. - Phonon and Raman scattering of two-dimensional transition metal dichalcogenides from monolayer, multilayer to bulk material. Chem. Soc. Rev., **44** (2015) 2757-2785. https://doi.org/10.1039/C4CS00282B.

53. Aliyev E., Filiz V., Khan M. M., Lee Y. J., Abetz C., Abetz V. - Structural characterization of graphene oxide: surface functional groups and fractionated oxidative debris. Nanomaterials, **9**(8) (2019) 1180. https://doi.org/10.3390/nano9081180.
54. Pang Y. L., Tee S. F., Lim S., Abdullah A. Z., Ong H. C., Wu C. H., Chong W. C., Mohammad A. W., Mahmoudi E. - Enhancement of photocatalytic degradation of organic dyes using ZnO decorated on reduced graphene oxide (rGO). Desalin. Water Treat., **108** (2018) 311-321. https://doi.org/10.5004/dwt.2018.21947.
55. Emiru T. F., Ayele D. W. - Controlled synthesis, characterization and reduction of graphene oxide: A convenient method for large scale production. Egypt. J. Basic Appl. Sci. **4** (2017) 74-79. https://doi.org/10.1016/j.ejbas.2016.11.002.
56. Ali M. E. M., Mohammed R., Abdel Moniem S. M., El Liethy M. A., Ibrahim H. S. - Green MoS_2 nanosheets as a promising material for decontamination of hexavalent chromium, pharmaceuticals, and microbial pathogen disinfection: spectroscopic study. J. Nanopart. Res., **24** (2022) 191. https://doi.org/10.1007/s11051-022-05573-6.
57. Liu Y., Zhao Y., Jiao L., Chen J. - A graphene-like MoS_2/graphene nanocomposite as a high-performance anode for lithium ion batteries. J. Mater. Chem. A, **2** (2014) 13109-13115. https://doi.org/10.1039/C4TA01644K.
58. Wiles D. M., Gingras B. A., Suprunchuk T. - The C=S stretching vibration in the infrared spectra of some thiosemicarbazones. Can. J. Chem., **45**(5) (1967) 469-473. https://doi.org/10.1139/v67-081.
59. Deng Z. H., Li L., Ding W., Xiong K., Wei Z. D. - Synthesized Ultrathin MoS_2 Nanosheets Perpendicular to Graphene for Catalysis of Hydrogen Evolution Reaction. Chem. Commun.**, 51** (2015) 1893-1896. https://doi.org/10.1039/C4CC08491H.
60. Teng Y., Zhao H., Zhang Z., Li Z., Xia Q., Zhang Y., Zhao L., Du X., Du Z., Lv P., Swierczek K. - MoS_2 nanosheets vertically grown on graphene sheets for lithium ion battery anodes. ACS Nano, **10**(9) (2016) 8526-8535. https://doi.org/10.1021/acsnano.6b03683.
61. Kee C. W. - Assignment of O-O and Mo=O stretching frequencies of molybdenum/tungsten complexes revisited. J. Chem., **2015** (2015) 439270-439279. https://doi.org/10.1155/2015/439270.
62. Ritika, Kaur M., Umar A., Mehta S. K., Singh S., Kansal S. K., Fouad H., Alothman O. Y. - Rapid solar-light driven superior photocatalytic degradation of methylene blue using MoS_2-ZnO heterostructure nanorods photocatalyst. Materials, **11**(11) (2018) 2254. https://doi.org/10.3390/ma11112254.
63. Mauge F., Lamotte J., Nesterenko N. S., Manoilova O., Tsyganenko A. A. - FTIR study of surface properties of unsupported MoS_2. Catal. Today, **70**(1) (2001) 271-284. https://doi.org/10.1016/S0920-5861(01)00423-0.
64. Wright C. J., Sampson C., Fraser D., Moyes R. B., Wells P. B., Riekel C. - Hydrogen sorption by molybdenum sulphide catalysts. J. Chem. Soc., Faraday Trans. 1, **76** (1980) 1585-1598. https://doi.org/10.1039/f19807601585.
65. Zhou X., Xu B., Lin Z., Shu D., Ma L. - Hydrothermal synthesis of flower-like MoS_2 nanospheres for electrochemical supercapacitors. J. Nanosci. Nanotechnol., **14**(9) (2014) 7250-7254. https://doi.org/10.1166/jnn.2014.8929.
66. Frindt R. F. - Single Crystals of MoS_2 Several Molecular Layers Thick. J. Appl. Phys., **37**(4) (1966) 1928-1929. https://doi.org/10.1063/1.1708627.
67. Ganguly A., Sharma S., Papakonstantinou P., Hamilton J. - Probing the thermal deoxygenation of graphene oxide using high-resolution in situ X-ray-based spectroscopies. J. Phys. Chem. C, **115** (2011) 17009-17019. https://doi.org/10.1021/jp203741y.
68. Gao J., Li B. C., Tan J. W., Chow P., Lu T. M., Koratkar N. - Aging of transition metal dichalcogenide monolayers. ACS Nano, **10** (2016) 2628-2635. https://doi.org/10.1021/acsnano.5b07677.
69. Lu Q., Yang Y., Feng J., Wang X. - Oxygen-defected molybdenum oxides hierarchical nanostructure constructed by atomic-level thickness nanosheets as an efficient absorber for solar steam generation. Sol. RRL, **3** (2019) 1800277. https://doi.org/10.1002/solr.201800277.
70. Li Z., Zhan X., Qi S. - A facile alkali metal hydroxide-assisted controlled and targeted synthesis of 1T MoS_2 single-crystal nanosheets for lithium ion battery anodes. Nanoscale, **11** (2019) 14857-14862. https://doi.org/10.1039/C9NR04537F.

71. Tang Y., Zhao Z., Wang Y., Dong Y., Liu Y., Wang X., Qiu J. - Ultrasmall MoS_2 nanosheets mosaiced into nitrogen-doped hierarchical porous carbon matrix for enhanced sodium storage performance. Electrochim. Acta, **225** (2017) 369-377. https://doi.org/10.1016/j.electacta.2016.12.176.
72. Wang Y., Sun S., Liu Y., Zhang Y., Xia J., Yang Q. - TiO_2 coupled to predominantly metallic MoS_2 for photocatalytic degradation of rhodamine B. J. Mater. Sci., **55** (2020) 12274-12286. https://doi.org/10.1007/s10853-020-04906-x.
73. Wang Z., Dong Y., Li H., Zhao Z., Bin Wu H., Hao C., Liu S., Qiu J., Lou X. W. - Enhancing lithium-sulphur battery performance by strongly binding the discharge products on amino-functionalized reduced graphene oxide. Nat. Commun., **5** (2014) 5002. https://doi.org/10.1038/ncomms6002.
74. Wei Z. Q., Dai X. C., Hou S., Li Y. B., Huang M. H., Li T., Xu S., Xiao F. X. - Branched polymer-incorporated multi-layered heterostructured photoanode: precisely tuning directional charge transfer toward solar water oxidation. J. Mater. Chem. A, **8** (2020) 177-189. https://doi.org/10.1039/C9TA11579J.
75. Xuyen N. T., Ting J. M. - Hybridized 1T/2H MoS_2 having controlled 1T concentrations and its use in supercapacitors. Chem. Eur. J., **23** (2017) 17348-17355. https://doi.org/10.1002/chem.201703690.
76. Chao Y., Jalili R., Ge Y., Wang C., Zheng T., Shu K., Wallace G. G. - Self-assembly of flexible free-standing 3D porous MoS_2-reduced graphene oxide structure for high-performance lithium-ion batteries. Adv. Funct. Mater., **27** (2017) 1700234. https://doi.org/10.1002/adfm.201700234.
77. Gao Z., Li M., Wang J., Zhu J., Zhao X., Huang H., Zhang J., Wu Y., Fu Y., Wang X. - Pt nanocrystals grown on three dimensional architectures made from graphene and MoS_2 nanosheets: highly efficient multifunctional electrocatalysts toward hydrogen evolution and methanol oxidation reactions. Carbon, **139** (2018) 369-377. https://doi.org/10.1016/j.carbon.2018.07.006.
78. Wang J. G., Liu H., Zhou R., Liu X., Wei B. - Onion-like nanospheres organized by carbon encapsulated few-layer MoS_2 nanosheets with enhanced lithium storage performance. J. Power Sources, **413** (2019) 327-333. https://doi.org/10.1016/j.jpowsour.2018.12.055.
79. Ohtaki H., Radnai T. - Structure and dynamics of hydrated ions. Chem. Rev., **93**(3) (1993) 1157-1204. https://doi.org/10.1021/cr00019a014.
80. Zhang F., Tang Y., Liu H., Ji H., Jiang C., Zhang J., Zhang X., Lee C. S. - Uniform incorporation of flocculent molybdenum disulfide nanostructure into three dimensional porous graphene as an anode for high-performance lithium ion batteries and hybrid supercapacitors. ACS Appl. Mater. Interfaces, **8** (2016) 4691-4699. https://doi.org/10.1021/acsami.5b11705.
81. Khawula T. N. Y., Raju K., Franklyn P. J., Sigalas I., Ozoemena K. I. - Symmetric pseudocapacitors based on molybdenum disulfide (MoS_2)-modified carbon nanospheres: correlating physicochemistry and synergistic interaction on energy storage. J. Mater. Chem. A, **4**(17) (2016) 6411-6425. https://doi.org/10.1039/C6TA00114A.
82. Wang C., Zhou J., Du F. - Synthesis of Highly Reduced Graphene Oxide for Supercapacitor. Journal of Nanomaterials, **2016** (2016) 4840301. https://doi.org/10.1155/2016/4840301.
83. Hu B., Qin X., Asiri A. M., Alamry K. A., Al-Youbi A. O., Sun X. - Synthesis of porous tubular C/MoS_2 nanocomposites and their application as a novel electrode material for supercapacitors with excellent cycling stability. Electrochim. Acta, **100** (2013) 24-28. https://doi.org/10.1016/j.electacta.2013.03.133.
84. Ali G. A. M., Thalji M. R., Soh W. C., Algarni H., Chong K. F. - One-step electrochemical synthesis of MoS_2/graphene composite for supercapacitor application. J. Solid State Electrochem., **24** (2020) 25-34. https://doi.org/10.1007/s10008-019-04449-5.
85. Wang R., Wang S., Peng X., Zhang Y., Jin D., Chu P. K., Zhang L. - Elucidating the intercalation pseudocapacitance mechanism of MoS_2-carbon monolayer interoverlapped superstructure: Toward high-performance sodium ion-based hybrid supercapacitor. ACS Appl. Mater. Interfaces, **9** (2017) 32745-32755. https://doi.org/10.1021/acsami.7b09813.
86. Sarkar D., Das D., Das S., Kumar A., Patil S., Nanda K. K., Sarma D. D. - Expanding interlayer spacing in MoS_2 for realizing an advanced supercapacitor. ACS Energy Lett., **4** (2019) 1602-1609. https://doi.org/10.1021/acsenergylett.9b00983.